Electronic
Research Archive

https://www.aimspress.com/journal/era

ERA, 34(7): 4999–5022.
DOI: 10.3934/era.2026221
Received: 06 February 2026
Revised: 24 May 2026
Accepted: 27 May 2026
Published: 10 June 2026

Research article

Thermal-resilient disturbance rejection control for high-speed maglev levitation systems

Fei Ni[1,2], **Cheng Tian**[1], **Donghua Wu**[3,4], **Junqi Xu**[1,2] **and Lijun Rong**[1,2,*]

[1] College of Transportation, Tongji University, Shanghai 201804, China
[2] National Maglev Transportation Engineering R&D Center, Tongji University, Shanghai 201804, China
[3] CRRC Qingdao Sifang Co., Ltd., Qingdao 266111, China
[4] State Key Laboratory of High-speed Maglev Transportation Technology, Qingdao 266111, China

* **Correspondence:** Email: ronglijun@tongji.edu.cn.

Abstract: Temperature-induced drift in the winding resistance of long-stator linear synchronous motors (LSLSMs) critically affects the levitation control performance of high-speed magnetic levitation (maglev) trains. To address this issue, this paper proposes a collaborative optimization framework that integrates multiphysics coupling analysis with active disturbance rejection control (ADRC). First, an electromagnetic-thermal-fluid coupling model of the LSLSM is developed through finite-element co-simulation. Second, a fast temperature prediction model is established by combining the parameter fitting with a lumped parameter thermal network (LPTN), enabling dynamic estimation of the winding temperature and the associated resistance drift. Third, an extended state observer (ESO) is employed to estimate and compensate for thermally induced parameter drift in real time. Numerical simulations under multiple operating scenarios show that the proposed method achieves improved tracking performance, stronger disturbance rejection capability, and better robustness against thermal-induced parameter drift than the benchmark proportional-integral-derivative (PID) controller. In addition, considering thermal-induced parameter drift in the controller design process leads to more consistent closed-loop performance in the levitation plant.

Keywords: maglev train; levitation system; long-stator linear synchronous motor; parameter drift; multiphysics coupling

1. Introduction

Benefiting from contactless motion, ultra-high operating speed, and low energy consumption, high-speed magnetic levitation (maglev) trains have become the core direction for next-generation rail transit [1, 2]. However, their levitation systems face a challenge in maintaining dynamic stability due to strong multiphysics coupling under high-speed conditions. Copper and iron losses in the long-stator linear synchronous motor (LSLSM) secondary cause a local temperature increase, altering the resistance of the winding. The interaction between electromagnetic force and levitation dynamics negatively affects the performance of the levitation control system [3]. Therefore, constructing a high-precision electromagnetic-thermal-fluid coupling model and designing a control algorithm with parameter drift suppression capability are the keys to breaking through the performance bottleneck of the levitation system.

In recent years, scholars have carried out a series of studies on multiphysics modeling and control design for high-speed maglev levitation systems. From the thermal-analysis perspective, existing studies have mainly focused on loss estimation, electromagnetic-thermal coupling, and fast temperature-rise prediction. For example, Guo et al. improved the cooling performance of permanent-magnet on-wheel motors through electromagnetic-thermal coupling analysis [4], Ma et al. developed a finite-element model for high-accuracy iron-loss calculation [5], and Cao et al. established a field-circuit coupling model to analyze the output characteristics of linear synchronous motors [6]. In terms of fast thermal prediction, Schmid et al. employed a lumped-parameter formulation to construct a simplified electromagnet model, providing a useful basis for dynamic temperature-response calculation [7]. These studies provide important tools for thermal characterization, but they mainly remain at the level of loss/temperature analysis, and the resulting temperature rise is rarely explicitly linked to a control-relevant parameter drift in the levitation plant.

More broadly, recent studies on coupled electromagnetic-fluid or multiphysical field modeling have further demonstrated the growing importance of control-oriented multiphysics analysis in intelligent electromechanical systems. For example, Wang et al. investigated the dynamic behavior of a magnetorheological damper in coupled multiphysical fields, showing how interactions among multiple physical domains affect system-level dynamic characteristics [8]. Similarly, Szelag et al. developed a coupled field model for a hybrid-excited magnetorheological fluid brake in which transient fluid dynamics, electromagnetic field, thermal field, and mechanical equilibrium were considered simultaneously [9]. Although these studies were not directly focused on high-speed maglev systems, they indicate that electromagnetic–fluid–thermal coupling has become an important modeling direction in advanced electromechanical applications. This broader context helps position the present work not only within maglev levitation control but also within the wider readership interested in multiphysics modeling and control-oriented analysis.

From a control perspective, existing methods can be broadly grouped into three categories. The first category is conventional fixed-gain control, typically represented by proportional-integral-derivative (PID)-based methods, which are attractive because of their simple structure and ease of implementation [10, 11]. However, such methods are inherently sensitive to plant-parameter variations and external disturbances, and their performance may significantly deteriorate under high-speed operating conditions [12]. The second category is the control based on the estimation of disturbance, represented by active disturbance rejection control (ADRC)-type strategies. Zhang and Wang et al. introduced ADRC into maglev systems and improved robustness through disturbance observation and compensation [13, 14]. These methods enhance the rejection of conventional disturbances, but the corresponding discussions are still mainly centered on external disturbances or nominal-model mismatch. The third category is model-assisted adaptive or composite disturbance-compensation methods. For example, adaptive fuzzy model-reference control has been developed for magnetic levitation systems, demonstrating the potential of adaptive intelligent control in improving tracking performance under model uncertainty [15]. Yang et al. proposed a model-dependent active disturbance rejection method, thereby integrating model reference adaptive control (MRAC) with ADRC, and verified its effectiveness under load disturbances [16]. This type of method further improves adaptability, yet its effectiveness under thermally induced, time-varying parameter drifts remains insufficiently clarified.

Therefore, the limitation of existing studies is not merely the absence of thermal analysis or robust control individually but rather the weak connection between them. Specifically, the literature lacks a unified framework that explicitly links temperature rise to winding resistance variation, then to electromagnetic actuation change, and finally to levitation control performance degradation. Consequently, although existing advanced strategies may effectively counteract conventional external disturbances, their capability to handle thermally induced, time-varying disturbances remains unclear. This gap motivates the present work.

This paper presents a robust levitation control framework for high-speed maglev trains. The principal contributions are as follows.

(1) Characterization of thermal-induced effects: control-oriented, sequentially coupled electromagnetic-thermal-fluid framework is established for spatiotemporal analysis of copper and iron losses in the windings and teeth of LSLSMs. On this basis, the physical chain from temperature rise to winding-resistance variation is explicitly characterized.

(2) Estimation of temperature-dependent quantities: a lumped parameter thermal network (LPTN)-based temperature prediction model with fitted nodal losses is proposed for rapid estimation of the thermal state of the secondary. This reduced-order model enables real-time prediction of control-relevant quantities, especially the winding temperature and the associated resistance drift.

(3) Design of thermal-resilient levitation control: an ADRC-based levitation controller incorporating an extended state observer (ESO) is developed for the maglev system with temperature-dependent parameters. By treating thermal-induced parameter drift as part of the total disturbance, the proposed method achieves improved robustness against time-varying thermal effects compared to conventional controllers.

The structure of this paper is organized as follows. Section 2 introduces the LSLSM, derives its thermal characteristics through finite element analysis, and establishes a fast temperature prediction model based on the LPTN framework. Section 3 formulates a nonlinear dynamic model of an electromagnet that incorporates thermal effects, followed by the design of an ADRC with systematic parameter tuning methodologies. Section 4 presents simulation results that validate the impact of thermal effects and highlight the superiority of the proposed control scheme. Finally, Section 5 concludes the article with key findings and future directions.

2. Thermal characteristics of the LSLSM secondary

2.1. Framework for multiphysics coupling

As depicted in Figure 1, the levitation system employs an LSLSM, whose configuration consists of a track-side primary and a vehicle-mounted secondary. In the present work, multiphysics analysis is not introduced as an end in itself but as a means of extracting the thermal variables that are most relevant to levitation control.

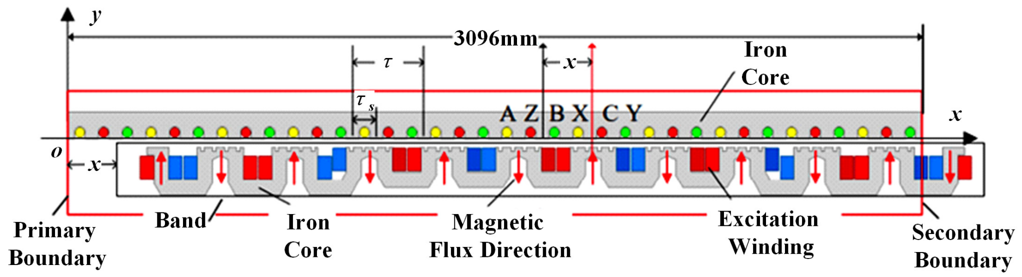

Figure 1. Finite element schematic of the LSLSM.

A one-way sequential Maxwell-Fluent coupling framework is adopted. First, transient electromagnetic analysis in ANSYS Maxwell is used to calculate the dominant heat sources in the secondary, namely the copper loss in the excitation winding and the iron loss in the laminated core. These losses are then mapped the ANSYS Fluent as volumetric heat sources to obtain the transient temperature field under convective cooling. The main role of multiphysics simulation is to provide four key outputs: (1) the spatial loss distribution in the secondary, (2) the temperature distribution of the secondary components, (3) the evolution of the winding temperature, and (4) the temperature-dependent winding resistance drift derived from the winding temperature.

To preserve physical fidelity while maintaining computational efficiency, the computational domain is restricted to the active coupling region surrounding the air gap and the secondary electromagnet. The model employs a 2D formulation in the x-y plane and neglects the end effects in the thermal analysis of the representative operating section. The adopted one-way coupling strategy captures the dominant electromagnetic-thermal pathway required for the present study while avoiding the excessive computational cost associated with fully iterative bidirectional coupling.

Consequently, the multiphysics framework serves two control-oriented purposes: first, to identify the major thermal source regions and their temperature evolution; second, to provide the reduced-order model with key control-relevant thermal quantities, especially the winding temperature that directly determines the resistance variation used later in the levitation-control model.

2.2. *Thermal analysis of secondary components*

The Shanghai maglev demonstration line adopts a segmented power supply strategy for the LSLSM. In this operating mode, thermal accumulation in the primary (guideway) is limited by the short energization duration, whereas the onboard secondary electromagnet experiences sustained excitation and therefore constitutes the dominant thermal object for control-oriented analysis. For this reason, the thermal study in this paper focuses on the levitation electromagnet mounted on the vehicle.

Electromagnetic analysis shows that the dominant heat sources in the secondary originate from two mechanisms: iron losses induced by slotting and harmonic effects in the laminated core, and copper losses generated by the direct current (DC) excitation winding. The resulting loss distribution is shown in Figure 2(a). It can be seen that the losses are predominantly concentrated in the tooth region and the winding region, whereas the yoke and the middle section exhibit a much lower loss intensity. This spatial nonuniformity is of direct importance for reduced-order thermal modeling because it determines how the secondary should be partitioned into thermally distinct nodes.

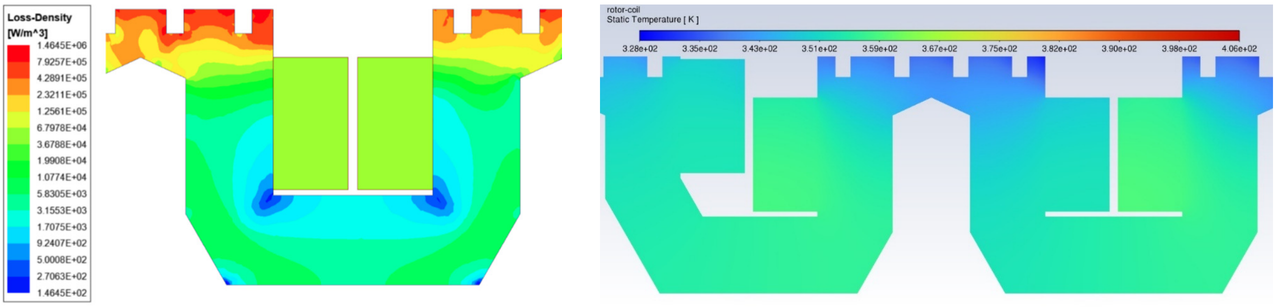

(a) Local loss contour map. **(b)** Local temperature cloud map.

Figure 2. Local loss contour map and local temperature cloud map of the LSLSM.

Based on the imported loss field, the temperature distribution is obtained using ANSYS Fluent, as shown in Figure 2(b). The thermal results reveal that the secondary does not behave as a uniform lumped body: the winding exhibits the highest temperature, the yoke and midsection experience delayed heat accumulation, and the tooth region remains relatively cooler because of stronger convective dissipation. These observations provide the physical basis for the nodal partitioning of the subsequent LPTN model.

For the purpose of levitation control, the most critical variable extracted from the temperature field is the winding temperature. This is because the winding temperature directly determines the resistance variation of the excitation circuit, which enters the levitation dynamics and acts as a temperature-induced time-varying parameter in the control model.

Accordingly, the multiphysics thermal simulation in this section is used not only to characterize the temperature field itself but also to identify the control-relevant variable pathway from loss distribution to winding temperature and then to resistance drift.

2.3. *Real-time estimation of winding temperature*

Although computational fluid dynamics (CFD) offers high-fidelity thermal modeling, its practical application is often limited by prohibitive computational demands and an extended runtime. Integrating CFD-based thermal analysis directly into the levitation control system would require repeated simulations for every operational change, making such an approach computationally prohibitive in practice. To overcome this limitation, this paper introduces a rapid prediction model for motor secondary temperature rise, developed through the integration of parameter fitting and an LPTN. This hybrid model enables real-time consideration of thermal effects in levitation control algorithms [17]. The implementation workflow is shown in Figure 3.

2.3.1. Loss parameter fitting

To quantitatively characterize secondary losses, a least-squares fitting method is used to correlate nodal losses with excitation current and train speed. Finite element simulations indicate that most losses are concentrated in the secondary teeth and windings, whereas the midsection and yoke exhibit much lower levels. For thermal and structural modeling, the secondary is discretized into four nodes: teeth, midsection, yoke, and windings. The winding losses are directly derived from the excitation

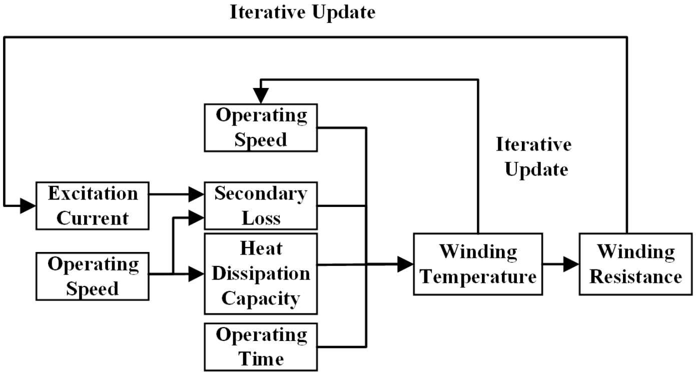

Figure 3. Implementation flowchart of the proposed temperature estimation strategy.

current, and the losses of the other three nodes are extracted from finite element simulations under various operating conditions and subsequently fitted using polynomial regression. Representative sampling points are selected across the teeth, midsection, yoke, and winding regions to ensure that the chosen nodes capture the spatial distribution of secondary losses effectively.

A comprehensive parameter sweep is performed using ANSYS Maxwell, with excitation currents ranging from 16 to 28 A in 2 A increments and operating speeds from 300 to 600 km/h in 100 km/h increments. For each resultant operating point, the nodal losses are spatially averaged and normalized to facilitate subsequent curve fitting. A third-order polynomial model is constructed to represent the nodal losses $f(x, y)$ as a function of the excitation current x and the operating speed y. Its general form is given by

$$\begin{aligned} f(x, y) = P_{00} + P_{10}x + P_{01}y + P_{20}x^2 + P_{11}xy + \\ P_{02}y^2 + P_{30}x^3 + P_{21}x^2y + P_{12}xy^2 + P_{03}y^3, \end{aligned} \tag{2.1}$$

where P_{ij} is the fitting coefficient (i, j= 0,1,2,3).

2.3.2. LPTN model formulation

To account for the specific motor geometry and cooling arrangement, a half-symmetry LPTN model is constructed for an individual levitation electromagnet, as illustrated in Figure 4.

The thermal model is formulated using an electrothermal analogy, whereby the temperatures are represented by node voltages, the heat fluxes by branch currents, and the thermal resistances model conductive and convective heat transfer paths. Conductive resistances are defined between solid components such as the tooth-yoke interfaces and the winding-core interfaces, whereas convective resistances are applied to exposed surfaces including the teeth and winding slots. Contact resistances at material interfaces are omitted on the basis of the effective mechanical bonding between the assembled components. Furthermore, in accordance with the modeling approach established in [18], the analysis incorporates the following assumptions: radial and axial heat conduction are treated as independent without cross-coupling, circumferential heat transfer is neglected, volumetric heat generation is uniform within each node, and the cooling air is considered isothermal.

Based on the thermal structure and loss distribution of the secondary electromagnet, the model is discretized into four representative nodes, each corresponding to a distinct thermal region. Node 1 corresponds to the secondary teeth, Node 2 to the midsection, Node 3 to the yoke, and Node 4 to the

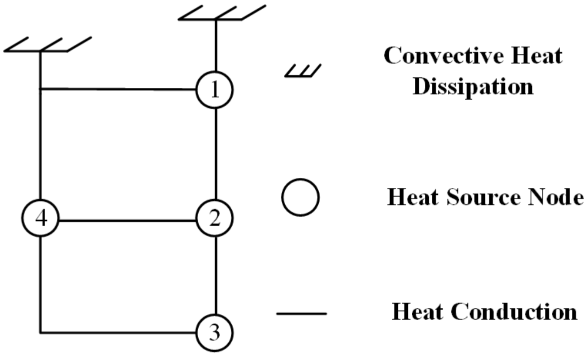

Figure 4. Four-node LPTN model of the LSLSM secondary. Node 1 represents the secondary teeth, Node 2 represents the midsection, Node 3 represents the yoke, and Node 4 represents the windings.

windings. The choice of a four-node discretization is motivated by both the thermal physics of the levitation electromagnet and the intended control-oriented application of the model.

First, the loss distribution obtained from the electromagnetic analysis shows that the teeth and windings are the main heat-generating regions, whereas the midsection and yoke exhibit comparatively lower but still distinguishable thermal behaviors. Meanwhile, these four regions differ in their thermal conduction path, local heat storage, and exposure to convective cooling. Therefore, they represent four thermally distinct subregions that should be retained in the reduced-order model.

Second, a coarser discretization with fewer nodes would merge regions with substantially different thermal characteristics. For example, combining the teeth and the yoke into a single iron-core node would smear out the strong temperature gradient between the locally heated tooth region and the more weakly cooled yoke region. Similarly, combining the winding with adjacent core regions would weaken the explicit representation of the winding temperature, which is the most control-relevant thermal variable in this work due to its direct effect on the temperature-dependent winding resistance.

Third, although a finer discretization with more nodes is possible, it would introduce additional thermal resistances, capacitances, and fitting parameters, thus increasing parameter-identification complexity and reducing computational efficiency. Because the purpose of the present LPTN is not to replace the full multiphysics solver but to provide a fast reduced-order predictor, the adopted four-node structure provides a suitable compromise between physical fidelity and computational efficiency.

The conductive thermal resistance is expressed as [19]

$$R_\lambda = \frac{L_i}{\lambda A_\lambda}, \tag{2.2}$$

where L_i is the conduction length, λ is the thermal conductivity, and A_λ is the cross-sectional area. The average convective heat transfer coefficient is determined as 388.8 $\mathrm{W/(m^2 \cdot {}^\circ C)}$.

Based on the principle of energy conservation, the nodal heat balance is expressed as

$$\mathbf{C}\dot{\boldsymbol{\theta}}(t) + \mathbf{G}\boldsymbol{\theta}(t) = \mathbf{Q}(t), \tag{2.3}$$

where $\mathbf{C}$ denotes the thermal capacitance matrix, $\mathbf{G}$ the thermal conductance matrix, $\mathbf{Q}(t)$ the heat input vector, and $\boldsymbol{\theta}(t)$ the nodal temperature vector.

Using the four-node thermal resistance network, the corresponding equation is formulated as shown in Eq (2.4).

$$\boldsymbol{A}\begin{pmatrix}\dot{T}_1\\ \dot{T}_2\\ \dot{T}_3\\ \dot{T}_4\end{pmatrix}+\boldsymbol{B}\begin{pmatrix}T_1\\ T_2\\ T_3\\ T_4\\ T_5\end{pmatrix}=\begin{pmatrix}P_1\\ P_2\\ P_3\\ P_4\end{pmatrix} \tag{2.4}$$

$$\boldsymbol{A}=\begin{pmatrix}C_1 & 0 & 0 & 0\\ 0 & C_2 & 0 & 0\\ 0 & 0 & C_3 & 0\\ 0 & 0 & 0 & C_4\end{pmatrix}$$

$$\boldsymbol{B}=\begin{pmatrix}G_{12}+G_{14}+G_{15} & -G_{12} & 0 & -G_{14} & -G_{15}\\ -G_{12} & G_{12}+G_{23}+G_{24} & -G_{23} & -G_{24} & 0\\ 0 & -G_{23} & G_{23}+G_{34} & -G_{34} & 0\\ -G_{14} & -G_{24} & -G_{34} & G_{14}+G_{24}+G_{34}+G_{45} & -G_{45}\end{pmatrix}$$

2.4. Validation of the thermal network model

2.4.1. Validation under nominal conditions

The developed thermal network model is used for the first time to calculate the increase in nodal temperature under the nominal operating conditions of a 20 A excitation current, a 600 km/h operating speed, and an ambient temperature of 20°C. As shown in Figure 5, the predicted nodal temperatures indicate that the windings are the hottest component, followed by the yoke, the middle section, and the teeth. This nominal condition result provides the baseline reduced-order thermal prediction used in the following analyses.

Based on the temperature-dependent resistance characteristics of the winding, the variation in its operational resistance during train operation can be quantified. This profile typically exhibits a progressive increase until a steady-state value is reached. The temperature dependence of the winding resistance is given by the following mathematical representation:

$$R(T) = R_0[1 + \alpha(T - T_0)], \tag{2.5}$$

where T denotes the current winding temperatur; e T_0 is the reference temperature (set to 20 °C); R_0 represents the corresponding baseline resistance; R is the resistance at temperature T; and α is the temperature coefficient of resistance, which is set to 0.004308 $°\mathrm{C}^{-1}$.

The results indicate that during train operation, the resistance to the winding increases progressively until it reaches a steady-state value, a process that coincides with the thermal equilibrium of all secondary components. Quantitatively, the winding resistance increases from its initial value of $0.4\,\Omega$ to $0.486\,\Omega$, representing an increase of 21.5%. This significant resistance drift may substantially impact controller performance and stability. When treated as a parametric disturbance, this resistance drift requires robust control strategies for effective compensation. The following section develops a temperature-aware levitation controller using ADRC, specifically designed to mitigate thermal effects on system performance.

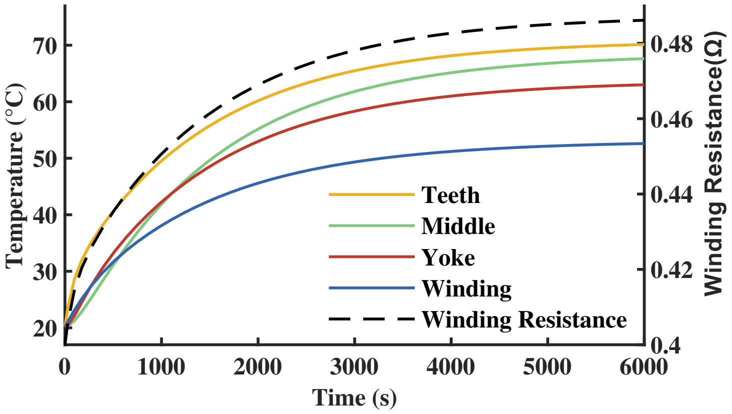

Figure 5. Estimated temperatures of nodal components and winding resistance values (referenced to 20°C ambient temperature).

2.4.2. Impact of the one-way coupling simplification

The present multiphysics framework adopts a one-way sequential Maxwell–Fluent coupling strategy in which temperature feedback to electromagnetic material properties is neglected during the electromagnetic loss calculation. To assess the influence of this simplification, an additional comparison is performed under a nominal operating condition of 600 km/h, 20 A excitation current, and 20°C ambient temperature. The nodal temperatures predicted by the one-way coupled model are compared with those obtained from the two-way coupled model, as summarized in Table 1.

The comparison shows that the two-way coupling changes the nodal temperatures only moderately under the operating condition considered. Specifically, the increase in the nodal temperature caused by the two-way coupling ranges from 0.5 K to 2.1 K, corresponding to a relative change of only 0.151%–0.632%.More importantly, for the winding node, which is the dominant thermal quantity relevant to control in the present work, the temperature rises from 332.7 K in the one-way case to 333.9 K in the two-way case, that is an increase of only 1.2 K (0.361%). According to Eq (2.5), the corresponding winding resistance changes from approximately 0.4684 Ω to 0.4705 Ω, which represents an additional increase of approximately 0.44%. These results indicate that the omission of temperature feedback mainly introduces a secondary correction to the thermal prediction, and winding-resistance drift remains the dominant thermally induced parameter variation affecting levitation performance.

It should be noted that this conclusion is valid for the operating range considered in this study. Two-way electromagnetic–thermal coupling may become more significant under extreme conditions, such as very high current densities, long-duration continuous operation, degraded cooling, or severe local saturation. In these cases, the temperature dependence of material properties may noticeably modify the electromagnetic losses, and the feedback from the thermal field to the electromagnetic field should be explicitly considered. Therefore, the one-way coupling strategy adopted in this work is suitable for control-oriented thermal estimation within the investigated operating range, whereas full two-way coupling is recommended for extreme thermal-stress or overload scenarios.

Table 1. Comparison of different coupling methods in predicting nodal temperature under nominal conditions.

Region	One-way (K)	Two-way (K)	ΔT (K)	Relative change (%)
Teeth	321.1	322.5	1.4	0.436
Midsection	330.5	331.0	0.5	0.151
Yoke	332.5	334.6	2.1	0.632
Winding	332.7	333.9	1.2	0.361

2.4.3. Validation under multiple conditions

To further assess the reliability of the reduced-order thermal model beyond the nominal condition, additional validation cases are considered by varying the ambient temperature and excitation current while keeping the train speed fixed at 600 km/h. The four-node LPTN is compared with the reference one-way coupled thermal solution, and the corresponding results are summarized in Table 2.

The results show that the proposed reduced-order thermal model maintains good agreement with the one-way coupled thermal solution across the considered temperature-current combinations. The total mean temperature relative error over all tested cases is 0.98%, and the maximum temperature relative error is limited to 2.711%. For the winding node, which is the thermal quantity most relevant to control in this study, the relative error of the winding temperature remains at or below 1.21% in all cases. These results indicate that the four-node LPTN can capture the dominant thermal behavior of the LSLSM secondary with satisfactory accuracy.

Table 2. Validation of the four-node LPTN against the one-way coupled thermal solution under multiple conditions.

Ambient temperature (°C)	Excitation current (A)	Mean temperature relative error (%)	Maximum temperature relative error (%)	Winding temperature relative error (%)
20	20	0.561	0.817	0.391
20	25	0.801	1.534	1.207
20	30	0.659	1.219	0.213
30	20	1.170	1.401	1.187
30	25	0.568	1.207	0.166
30	30	2.122	2.711	1.019

3. The proposed levitation control framework

3.1. Electromagnetic levitation system model

The single-point electromagnetic levitation system serves as the fundamental control unit for the entire levitation system. In this work, a nonlinear dynamic model of this representative system is established, which forms the basis for the multiphysics coupled optimization study of levitation control [7, 20]. The structural configuration of this single-point levitation system is presented in Figure 6, in which $c(t)$ is the levitation gap between the magnetic pole and the guide rail, $h(t)$ is the displacement of the track surface from the absolute reference plane, and $z(t)$ is the surface position of the magnetic pole relative to the reference plane.

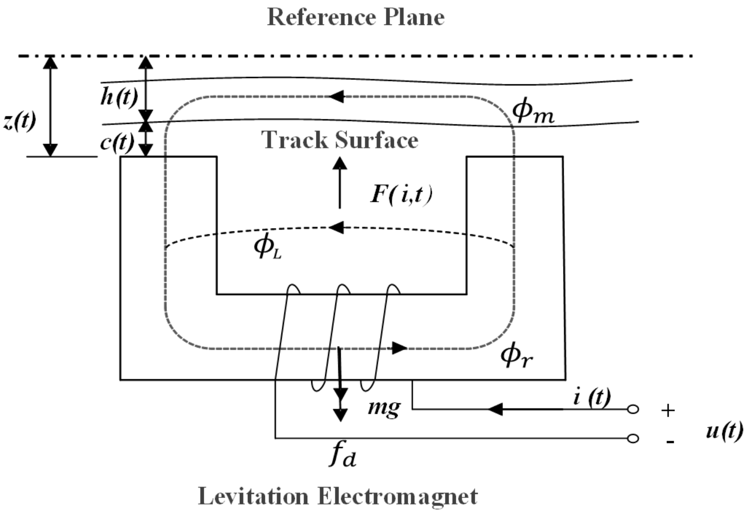

Figure 6. Structure of the single-point levitation system.

To maintain physical fidelity while reducing complexity, this study incorporates two assumptions [21]: (1) the ferromagnetic material in the electromagnetic circuit exhibits infinite permeability, and the magnetomotive force drops uniformly across the levitation gap; and (2) The leakage flux is negligible ($\phi_L = 0$). These simplifications enable tractable dynamics derivation while preserving essential system behavior.

Note that these assumptions are mainly introduced to derive a control-oriented levitation model. Under normal operating conditions, they provide a tractable approximation for controller design. However, under extreme operating conditions, such as very high excitation current, severe magnetic saturation, large air-gap variation, or pronounced leakage flux, the actual magnetic circuit may deviate from the idealized model. The infinite-permeability assumption may overestimate the useful air-gap flux and electromagnetic force for a given current, and neglecting leakage flux may further overestimate the effective force-producing flux. Consequently, when the model is extrapolated to such extreme conditions, it can underestimate the current required to maintain the desired levitation force, leading to an underestimate of copper loss, the rise of the winding temperature, and the corresponding thermally induced resistance drift. Therefore, in high-saturation or strong-leakage scenarios, a refined magnetic-circuit model or finite-element-based correction would be required for higher accuracy.

The dynamics of the single-point levitation system is derived from fundamental electromagnetic and mechanical principles. Combining electromagnetic winding dynamics (circuit behavior) with vertical motion dynamics (mechanical behavior) yields the following governing system equations:

$$\begin{cases} -\dfrac{\mu_0 N^2 A}{4}\left[\dfrac{i(t)}{c(t)}\right]^2 + mg + f_{\mathrm{d}}(t) = m\ddot{c}(t), \\ u(t) = R(T)i(t) + \dfrac{\mu_0 N^2 A}{2c(t)}\dot{i}(t) - \dfrac{\mu_0 N^2 A i(t)}{2c^2(t)}\dot{c}(t), \end{cases} \tag{3.1}$$

where N is the number of turns in the electromagnetic coil, A is the cross-sectional area of the iron core pole, $i(t)$ is the time-varying excitation current, μ_0 is the permeability of the free space, m is the equivalent mass of the levitation electromagnet, and $f_{\mathrm{d}}(t)$ is the external disturbance force.

Defining state variables as $x_1(t) = c(t)$, $x_2(t) = \dot{c}(t)$, and $x_3(t) = i(t)$, the dynamics of the levitation system in (3.1) can be transformed into the following state-space form:

$$\begin{cases} \dot{x}_1 = x_2, \\ \dot{x}_2 = -\dfrac{C}{m}\left[\dfrac{x_3}{x_1}\right]^2 + g - \dfrac{f_{\mathrm{d}}}{m}, \\ \dot{x}_3 = \dfrac{x_3 x_2}{x_1} - \dfrac{R(T)x_1 x_3}{2C} + \dfrac{x_1 u}{2C}, \end{cases} \tag{3.2}$$

where $C = \mu_0 N^2 A/4$ is the electromagnetic coupling constant, and $R(T)$ is the temperature-dependent winding resistance given by (2.5).

3.2. Active disturbance rejection control

For ADRC design, the control output is the levitation gap:

$$y = x_1 = c(t). \tag{3.3}$$

Then, from (3.2), its first- and second-order derivatives can be written as

$$\dot{y} = x_2, \tag{3.4}$$

$$\ddot{y} = -\frac{C}{m}\left(\frac{x_3}{x_1}\right)^2 + g - \frac{f_{\mathrm{d}}}{m}. \tag{3.5}$$

Differentiating (3.5) with respect to time and substituting $\dot{x}_3$ from (3.2), the third-order derivative of the output is obtained as

$$\dddot{y} = \frac{R(T)x_3^2}{mx_1} - \frac{\dot{f}_{\mathrm{d}}}{m} - \frac{x_3}{mx_1}u = \varphi(x,t) + b(x)u, \tag{3.6}$$

where

$$\varphi(x,t) = \frac{R(T)x_3^2}{mx_1} - \frac{\dot{f}_{\mathrm{d}}}{m}, \qquad b(x) = -\frac{x_3}{mx_1}. \tag{3.7}$$

Equation (3.6) shows that the original nonlinear electromechanical model has a relative degree of three with respect to the output $y = c(t)$. However, both $\varphi(x,t)$ and $b(x)$ contain nonlinear terms, thermally induced parameter drift, and external disturbances, making direct model-based compensation difficult. Following the standard ADRC philosophy, a constant nominal input gain b_0 is introduced, and the mismatch between $b(x)$ and b_0, together with the remaining nonlinear dynamics and external disturbances, is lumped into a total disturbance term,

$$f_t = \varphi(x, t) + (b(x) - b_0)u. \tag{3.8}$$

Hence, the system can be rewritten in the control-oriented canonical form

$$\dddot{y} = f_t + b_0 u. \tag{3.9}$$

By introducing the transformed states

$$\xi_1 = y, \qquad \xi_2 = \dot{y}, \qquad \xi_3 = \ddot{y}, \qquad \xi_4 = f_t, \tag{3.10}$$

the levitation system is reformulated into the third-order integral-chain form augmented by the disturbance state

$$\begin{cases} \dot{\xi}_1 = \xi_2, \\ \dot{\xi}_2 = \xi_3, \\ \dot{\xi}_3 = \xi_4 + b_0 u, \\ \dot{\xi}_4 = \dot{f}_t. \end{cases} \tag{3.11}$$

This reformulation provides an explicit transition from the nonlinear physical model to the ADRC structure so that a fourth-order ESO can be employed to estimate the transformed states and the lumped total disturbance in real time. The ADRC framework consists of three key components [22, 23]:

1) The tracking differentiator (TD), which arranges a smooth transition process for the reference signal and generates its differential.
2) The ESO, which estimates the transformed states of the integral-chain model together with the total disturbance.
3) The state error feedback controller (SEF), which generates the nominal control action according to the tracking error of the transformed states and then compensates for the estimated total disturbance through the observer output.

Designed in this way, ADRC does not require an exact inversion of the nonlinear electromagnetic levitation model. Instead, it treats the uncertain thermal-electromechanical effects as part of the total disturbance and suppresses them through dynamic estimation and compensation [24].

3.3. Levitation control under thermal effects

The ADRC applied to the single-point levitation system consists of the controlled plant and the three elements introduced above. In this framework, the reference gap r is input to the controller. Because the physical model has been reformulated in integral-chain form in (3.11), the ESO is designed to estimate four transformed states: the levitation gap ξ_1, its rate ξ_2, its equivalent acceleration ξ_3, and the lumped disturbance ξ_4. Therefore, the observer is constructed in control-oriented coordinates rather than by directly taking the physical excitation current as the third observer state.

3.3.1. Thermal effects on levitation systems

The thermal analysis in Section 2 shows that the winding temperature continuously increases during operation and directly causes resistance drift through the temperature-dependent relation in (2.5). In the levitation model, this thermal effect is not an external post-processing quantity but an intrinsic parameter variation that explicitly enters the electromechanical dynamics.

In particular, the third state equation in (3.2) shows that

$$\dot{x}_3 = \frac{x_3 x_2}{x_1} - \frac{R(T) x_1 x_3}{2C} + \frac{x_1 u}{2C}, \tag{3.12}$$

where $x_1 = c(t)$, $x_2 = \dot{c}(t)$, $x_3 = i(t)$, and $C = \mu_0 N^2 A/4$. It can be seen from (3.12) that an increase in $R(T)$ strengthens the resistance-related dissipation term $-R(T)x_1x_3/(2C)$. Under the same control input $u(t)$ and levitation gap $c(t)$, the excitation current rises more slowly, and the effective electromagnetic actuation is weakened.

Because the electromagnetic levitation force is proportional to the square of the current-to-gap ratio, the temperature-induced increase in winding resistance further propagates into the force-generation mechanism. In other words, the thermal effect first modifies the electrical parameter $R(T)$, then alters the current dynamics, and finally affects the electromagnetic force response and the closed-loop control performance. Therefore, the winding-resistance drift caused by the temperature rise should be interpreted as a control-relevant thermally induced parameter variation.

3.3.2. Design of the ESO

For the third-order integral-chain model in (3.11), a fourth-order ESO is implemented to estimate the three transformed states and the lumped disturbance:

$$\begin{cases} e = z_1 - y, \\ \dot{z}_1 = z_2 - \beta_1 e, \\ \dot{z}_2 = z_3 - \beta_2 e, \\ \dot{z}_3 = z_4 - \beta_3 e + b_0 u, \\ \dot{z}_4 = -\beta_4 e, \end{cases} \tag{3.13}$$

where z_1, z_2, z_3, and z_4 are the observations of ξ_1, ξ_2, ξ_3, and ξ_4, respectively, and β_1–β_4 are the gains of the observer. The characteristic equation of the fourth-order ESO (3.13) can be written as

$$L_{\mathrm{LESO}}(s) = s^4 + \beta_1 s^3 + \beta_2 s^2 + \beta_3 s + \beta_4. \tag{3.14}$$

The ESO design employs a single-parameter tuning strategy by assigning all observer poles to $-\omega_o$, where ω_o denotes the observer bandwidth. Accordingly, the characteristic polynomial is selected as

$$L_{\mathrm{LESO}}(s) = (s + \omega_o)^4. \tag{3.15}$$

By comparing (3.14) and (3.15), observer gains are obtained from binomial coefficients as

$$\beta_i = \binom{4}{i} \omega_o^i, \qquad i = 1, 2, 3, 4, \tag{3.16}$$

that is,

$$\beta_1 = 4\omega_o, \quad \beta_2 = 6\omega_o^2, \quad \beta_3 = 4\omega_o^3, \quad \beta_4 = \omega_o^4. \tag{3.17}$$

3.3.3. Design of the SEF

To maintain a simple control structure while preserving the disturbance rejection capability, a linear state-error feedback law is adopted for the nominal control action:

$$u_0 = -\frac{1}{b_0}\left[a_1(z_1 - r) + a_2 z_2 + a_3 z_3\right]. \tag{3.18}$$

The final control input is then obtained by compensating for the estimated total disturbance:

$$u = u_0 - \frac{z_4}{b_0}, \tag{3.19}$$

where z_1, z_2, z_3 are the observer estimates of transformed states, and z_4 is the estimate of the lumped disturbance. By assigning the closed-loop poles of the nominal error dynamics to $-\omega_c$, the feedback gains a_i $(i = 1, 2, 3)$ are determined by parameterizing the bandwidth as

$$a_i = \binom{3}{i-1}\omega_c^{4-i}, \qquad i = 1, 2, 3, \tag{3.20}$$

that is,

$$a_1 = \omega_c^3, \qquad a_2 = 3\omega_c^2, \qquad a_3 = 3\omega_c, \tag{3.21}$$

where ω_c represents the controller bandwidth.

4. Simulation results

In this section, numerical simulations are conducted to examine both the thermal behavior of the LSLSM secondary and the control performance of the proposed method. The study includes thermal characterization under multiple operating conditions, reference-tracking performance, robustness to thermal effects, robustness to composite disturbances, and a comparative evaluation of closed-loop performance under different thermal-model settings.

All simulations are performed based on the temperature-dependent single-point levitation model established in Section 3 with an initial levitation gap of 10 mm. The main parameters used in the simulations are the following: vacuum permeability $\mu_0 = 4\pi \times 10^{-7}$ H/m, reference gap $r = 8$ mm, nominal winding resistance $R_0 = 0.4\ \Omega$, effective pole-face area $A = 0.019\ \text{m}^2$, and equivalent levitated mass $m = 750$ kg. In addition, control performance is assessed by the following indices:

$$\begin{cases} \text{ISE} = \displaystyle\int_{t_0}^{t_1} |e(t)|^2\, dt, \\ \text{IAE} = \displaystyle\int_{t_0}^{t_1} |e(t)|\, dt, \\ \text{ITSE} = \displaystyle\int_{t_0}^{t_1} t\,|e(t)|^2\, dt, \\ \text{ITAE} = \displaystyle\int_{t_0}^{t_1} t\,|e(t)|\, dt, \end{cases} \tag{4.1}$$

where $e(t)$ denotes the tracking error of the levitation system, and $[t_0, t_1]$ is the evaluation time interval.

The ADRC and PID are tuned by particle swarm optimization (PSO) with the integral of time and absolute error (ITAE) as the objective function under identical optimization settings, namely a population size of 50, 200 iterations, and an inertia weight of 0.8. The ADRC parameters converge after about 180 generations, whereas the PID stabilizes within about 80 generations because of its lower dimensionality.

It should be noted that the PID gains listed in Table 3 are obtained by PSO optimization under the prescribed input-saturation constraint. The same saturation limit is imposed on both PID and ADRC during simulation. Therefore, although the optimized PID gains are numerically large, the actual control input applied to the levitation plant remains bounded by the actuator limit. The large gain values indicate that the fixed-gain PID requires relatively aggressive tuning to obtain competitive tracking performance for the nonlinear levitation system. Nevertheless, practical implementation would still require actuator-specific verification and gain rescaling according to the actual power-electronic and current-loop constraints.

For clarity, the resulting controller parameters are summarized in Table 3.

Table 3. Parameters of the proposed ADRC and PID.

Controller	Parameter	Symbol	Value
ADRC	ESO bandwidth	ω_o	280.63
	SEF bandwidth	ω_c	38.14
	Compensation factor	b_0	1.53
PID	Proportional gain	k_p	251090
	Integral gain	k_i	593500
	Derivative gain	k_d	5444

4.1. Characterization of thermal effects

To investigate the behavior of temperature rise under various operating conditions, numerical simulations are performed for multiple train speeds (300, 400, 500, and 600 km/h) and ambient temperatures (20°C and 40°C). The analysis focuses exclusively on thermal behavior by excluding other disturbance sources, and each simulation is run for 3600 s to capture the temperature evolution.

The results in Figure 7 reveal three main thermal characteristics. First, as the speed of the train increases, the secondary loss increases, which accelerates the increase in the winding temperature and increases the final winding temperature. Second, a higher ambient temperature reduces the effectiveness of convective cooling and therefore leads to a further increase in temperature. Third, after 3600 s of operation, the winding resistance increases by 17% and 25% at initial ambient temperatures of 20°C and 40°C, respectively.

These thermal effects are directly relevant for levitation control because the winding temperature affects the resistance of the levitation electromagnet through the temperature-dependent relation in Eq (2.5). Therefore, the temperature rise shown in Figure 7 does not simply represent a thermal phenomenon but directly induces the parameter drift in the levitation model through the increase of $R(T)$.

As discussed in Section 3.3.1, the temperature-dependent resistance enters the levitation-current dynamics explicitly and further propagates to the electromagnetic force-generation process. Therefore,

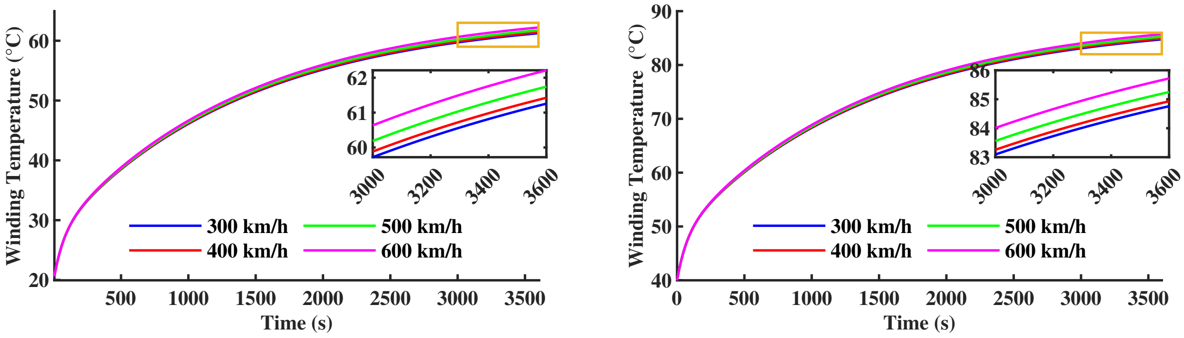

(a) The initial ambient temperature is 20°C.

(b) The initial ambient temperature is 40°C.

Figure 7. Time-domain evolution of winding temperature during operation.

the thermal effect should be interpreted as a control-relevant source of thermally induced parameter drift rather than merely a passive thermal by-product.

4.2. Verification of levitation control performance

4.2.1. Reference tracking

To assess tracking performance, the proposed control method is benchmarked against a PID controller under a step reference signal. The other simulation conditions are set as follows: a constant train speed of 600 km/h, a reference levitation gap of 8 mm, an initial ambient temperature of 20°C, and a simulation duration of 10 s. The step signal is defined as

$$r(t) = \begin{cases} 8\ \text{mm}, & 0 \leq t \leq 5\ \text{s}, \\ 10\ \text{mm}, & 5\ \text{s} \leq t \leq 10\ \text{s}. \end{cases} \tag{4.2}$$

The levitation-gap responses are shown in Figure 8(a). Compared with PID, the proposed ADRC exhibits a smaller overshoot, shorter convergence time, and superior dynamic tracking capability. It should be noted that the train speed is fixed at 600 km/h in this subsection because the objective here is to compare the baseline tracking capacity of the two controllers under the target operating scenario considered in this work rather than to perform a full speed-sensitivity study.

4.2.2. Robustness to thermal effects

To evaluate the robustness of the proposed control method against thermally induced parameter drift, a scenario is considered in which the train passes through a region with a significant ambient temperature change, such as a tunnel. An abrupt drop in ambient temperature from 40°C to 20°C is introduced at t = 5 s to emulate a sudden thermal transition. The other simulation conditions are set as follows: a constant train speed of 600 km/h, a reference levitation gap of 8 mm, no additional external disturbance, and a total simulation duration of 10 s. For comparison, the benchmark PID is evaluated under the same operating conditions.

The levitation-gap responses are shown in Figure 8(b). It can be observed that both controllers maintain stable levitation throughout the thermal transition, and the levitation gap remains very close

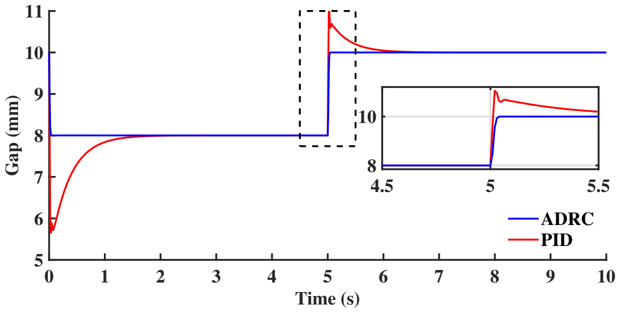

(**a**) Levitation gap under step reference signal.

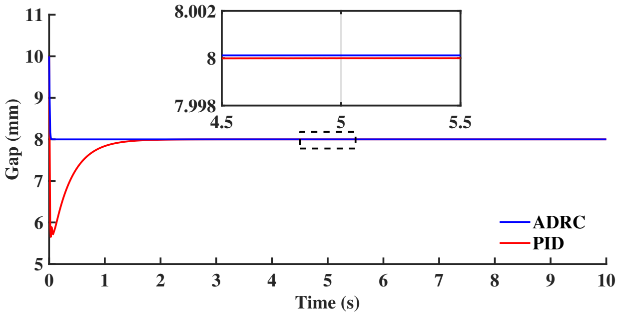

(**b**) Levitation gap responses of ADRC and PID under ambient temperature change.

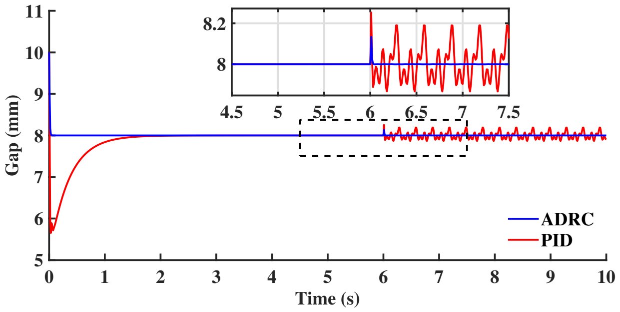

(**c**) Levitation gap responses of ADRC and PID under ambient temperature change and track irregularities.

Figure 8. Levitation-gap responses under different operating conditions.

to the nominal value of 8 mm throughout the simulation interval. This indicates that the abrupt ambient temperature change introduces only a very small perturbation to the closed-loop response under the tested operating condition.

The enlarged local view around $t = 5$ s is included only to make this minute deviation more visible. As shown in the inset, the response difference between the two controllers remains small even after magnification. Compared with the PID, the proposed ADRC exhibits a slightly smoother local response immediately after the temperature jump; however, the overall deviation magnitude is limited for both controllers.

Overall, the results indicate that both the ADRC and PID can maintain high-precision gap regulation under sudden thermally induced parameter drift. More importantly, Figure 8b suggests that the direct influence of the abrupt thermal transition on the levitation gap is small in magnitude, although ADRC shows a slight advantage in local smoothness under the tested conditions.

4.2.3. Robustness to composite disturbances

To evaluate the robustness of the proposed control method under composite disturbances, an abrupt ambient temperature change is further combined with multifrequency track-irregularity excitation, and the resulting response is compared with that of the benchmark PID. The simulation conditions are set as follows: a constant train speed of 600 km/h; a reference levitation gap of 8 mm; an initial ambient temperature of 40°C, which drops abruptly to 20°C at $t = 5$ s; and a total simulation duration of 10 s. To distinguish the effects of different disturbance sources more clearly, the simulation is divided into three stages: 0–5 s for nominal steady operation without disturbance, 5–6 s for the response to abrupt ambient temperature change, and 6–10 s for the composite disturbance response under the simultaneous action of abrupt ambient temperature change and multifrequency track irregularity.

The introduced track irregularities are given by [25]

$$d(t) = \begin{cases} 0, & 0 \le t < 6 \text{ s}, \\ 0.8\sin(6.72\pi t) + 0.3\sin(13.44\pi t + \pi/6) + 0.1\sin(20.16\pi t + \pi/4) \text{ mm}, & 6 \le t \le 10 \text{ s}. \end{cases} \tag{4.3}$$

The levitation-gap responses under combined ambient temperature change and track irregularities are presented in Figure 8(c). It can be seen that, after the abrupt drop in ambient temperature at $t = 5$ s, both controllers experience a small transient deviation. This deviation is induced by the thermally induced parameter drift associated with the sudden change in ambient temperature. After the multifrequency track-irregularity excitation is introduced at $t = 6$ s, the difference between the two methods becomes much more pronounced: The proposed ADRC maintains a smaller fluctuation range and faster recovery capability, whereas the PID exhibits more obvious oscillation and accumulated tracking error.

The quantitative comparison in Table 4 further confirms this observation. It can be found that the proposed ADRC outperforms the PID in all four performance indices. Specifically, compared to the PID, the integral squared error (ISE), integral absolute error (IAE), integral time squared error (ITSE), and ITAE of ADRC are reduced by approximately 97.8%, 97.9%, 99.4%, and 99.0%, respectively. This indicates that the proposed controller not only retains a clear advantage in suppressing instantaneous errors but also achieves substantially better long-term accumulated tracking performance. Therefore, under the simultaneous action of abrupt ambient temperature change and multifrequency track irregularity, the ADRC demonstrates substantially stronger composite disturbance rejection capability than the benchmark PID.

4.3. Influence of thermal effects on control performance

To investigate the impact of thermal effects on levitation control performance, a comparative study is conducted on the levitation system in two controller design settings. In the first setting, the controller parameters are determined by accounting for thermally induced parameter drift via the temperature-dependent winding resistance. In the second setting, the drift is ignored. Both controllers are evaluated under realistic operating conditions to compare their closed-loop performance.

The assessment employs a square-wave reference signal in which the levitation gap alternates between 8 mm and 10 mm, corresponding to a variation of 2 mm with a period of 50 s. For the main comparison of thermal effects, the operating conditions are set as follows: a speed of 600 km/h, an

Table 4. Performance metrics of different control algorithms under composite disturbances.

Algorithm	Metric	Value
ADRC	ISE ($\mathrm{mm}^2{\cdot}\mathrm{s}$)	2.874×10^{-8}
	IAE ($\mathrm{mm}{\cdot}\mathrm{s}$)	2.586×10^{-5}
	ITSE ($\mathrm{mm}^2{\cdot}\mathrm{s}^2$)	3.149×10^{-9}
	ITAE ($\mathrm{mm}{\cdot}\mathrm{s}^2$)	2.656×10^{-5}
PID	ISE ($\mathrm{mm}^2{\cdot}\mathrm{s}$)	1.304×10^{-6}
	IAE ($\mathrm{mm}{\cdot}\mathrm{s}$)	1.253×10^{-3}
	ITSE ($\mathrm{mm}^2{\cdot}\mathrm{s}^2$)	4.978×10^{-7}
	ITAE ($\mathrm{mm}{\cdot}\mathrm{s}^2$)	2.676×10^{-3}

ambient temperature of 20°C, and a simulation duration of 3600 s. To further examine the consistency of control performance at a lower representative speed, an additional case at 400 km/h is considered under the same square-wave reference setting. The reference signal is defined as

$$r(t) = \begin{cases} 8\ \mathrm{mm}, & 25k \le t \le 25(2k+1), \\ 10\ \mathrm{mm}, & 25(2k+1) \le t \le 25(2k+2), \end{cases} \tag{4.4}$$

where $k \in \mathbb{N}_0$ denotes the discrete-time index, and t denotes the simulation time in seconds.

Table 5 summarizes the quantitative performance metrics under the representative operating speeds. The 600 km/h cases are used as the main comparison to evaluate the influence of considering thermally induced parameter drift in controller design, and the 400 km/h cases are included to examine whether the control performance trend remains consistent at a lower speed. Because the raw values of different indices vary significantly in magnitude, the 600 km/h performance indices are normalized by the corresponding ADRC values obtained from the controller design that ignores thermally induced parameter drift. The normalized results are presented in Figure 9.

Table 5 and Figure 9 show that incorporating thermally induced parameter drift into the ADRC design improves all four performance indices at 600 km/h. Specifically, compared to the ADRC design that ignores the drift, the design that accounts for the drift reduces ISE, IAE, ITSE, and ITAE by approximately 29.4%, 21.2%, 29.2%, and 18.9%, respectively. These results demonstrate that considering thermally induced parameter drift in ADRC design improves both short-term tracking quality and long-term accumulated error performance under realistic thermal operating conditions.

For the benchmark PID, considering thermally induced parameter drift, it improves IAE and ITAE but increases ISE and ITSE. This difference is mainly related to the different weighting characteristics of these performance indices. The absolute error indices, IAE and ITAE, accumulate the magnitude of the tracking error over the full operating interval and are therefore more sensitive to long-duration bias. In contrast, ISE and ITSE square the tracking error, so short-duration deviations with relatively larger amplitudes can contribute disproportionately to these indices. Therefore, a reduction in long-term accumulated absolute error does not necessarily lead to a reduction in the squared-error indices. This result suggests that, for the fixed-gain PID controller, considering thermal drift can improve part of the long-term tracking behavior, but it does not guarantee simultaneous improvement in all error metrics.

The results at 400 km/h show a performance trend consistent with that at 600 km/h. For the ADRC, considering thermally induced parameter drift reduces ISE, IAE, ITSE, and ITAE by approximately 14.4%, 12.7%, 14.9%, and 15.8%, respectively, compared to the design that ignores thermal effects. In the thermally aware design setting, the ADRC also achieves lower ISE, IAE, ITSE, and ITAE compared to the PID. Specifically, compared to the PID, the ADRC reduces the four indices by approximately 75.0%, 88.8%, 74.5%, and 88.4%, respectively. This indicates that the performance advantage of the ADRC is maintained at different representative operating speeds.

Overall, the ADRC achieves better absolute performance than the PID in the design settings considered and representative operating speeds. In addition, compared to the PID, the ADRC benefits more consistently from incorporating thermally induced parameter drift into the controller design. These results support the need to incorporate thermal effects into the controller design process, especially for the proposed ADRC-based levitation control framework.

Table 5. Performance comparison of different levitation control designs under representative operating speeds.

Operating speed (km/h)	Controller design	Algorithm	ISE ($mm^2 \cdot s$)	IAE ($mm \cdot s$)	ITSE ($mm^2 \cdot s^2$)	ITAE ($mm \cdot s^2$)
400	Considering thermal effects	ADRC	5.252×10^{-6}	0.004399	0.009404	8.191
400	Ignoring thermal effects	ADRC	6.137×10^{-6}	0.00504	0.01105	9.729
400	Considering thermal effects	PID	2.104×10^{-5}	0.03938	0.03685	70.32
400	Ignoring thermal effects	PID	1.136×10^{-5}	0.08589	0.02045	156.6
600	Considering thermal effects	ADRC	5.252×10^{-6}	0.004339	0.009403	7.978
600	Ignoring thermal effects	ADRC	7.441×10^{-6}	0.005509	0.01329	9.841
600	Considering thermal effects	PID	2.353×10^{-5}	0.04610	0.04084	82.04
600	Ignoring thermal effects	PID	1.079×10^{-5}	0.08332	0.01907	150.3

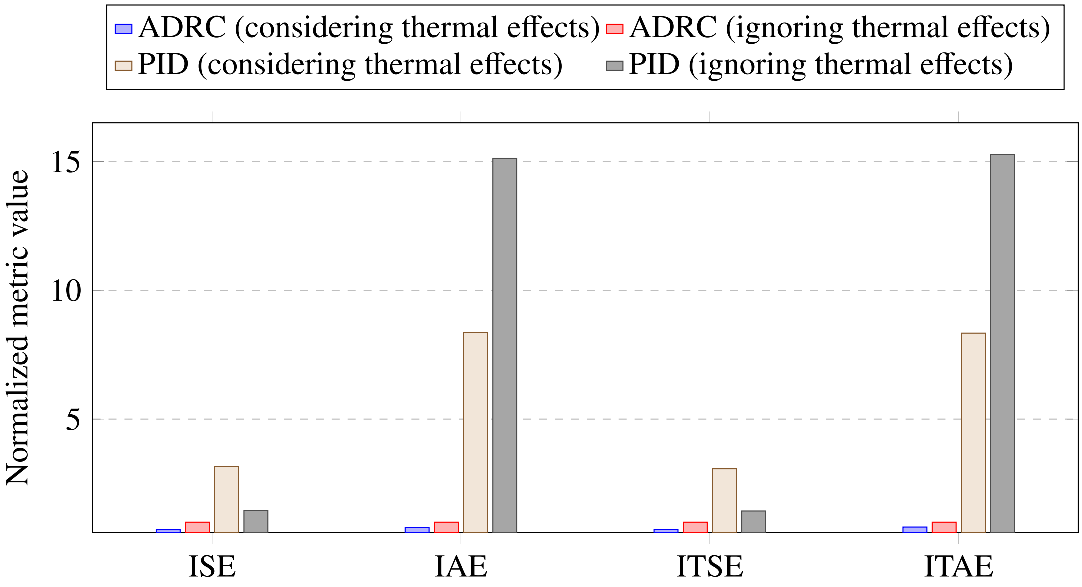

Figure 9. Normalized performance metrics of different levitation control designs at 600 km/h. Each metric is normalized by the corresponding ADRC value obtained under the design that ignores thermally induced parameter drift.

5. Conclusions

This paper investigates the degradation of levitation control in high-speed maglev trains caused by thermally induced parameter drift in the LSLSM secondary. To address this problem, an integrated framework is proposed that combines multiphysics thermal analysis, reduced-order temperature prediction, and ADRC-based levitation control. The main conclusions are summarized as follows.

(1) A control-oriented electromagnetic-thermal-fluid coupling framework is established through the cosimulation of ANSYS Maxwell and Fluent. The analysis identifies the secondary teeth and the windings as the dominant heat source regions. On this basis, a reduced-order thermal model is developed by combining data fitting with a four-node LPTN, enabling efficient prediction of the winding temperature and the associated resistance drift.

(2) A nonlinear single-point levitation dynamic model with temperature-dependent winding resistance is established. By reformulating the levitation dynamics into an integral chain form and incorporating an ESO into the ADRC framework, thermal-induced parameter drift can be treated as part of the total disturbance and compensated in real time.

(3) Numerical simulations under multiple operating scenarios show that the proposed approach achieves superior tracking performance, stronger disturbance rejection capability, and improved robustness against thermal effects compared to the benchmark controller. In addition, the results of Section 4.3 show that considering thermal-induced parameter drift in controller design leads to more consistent closed-loop performance, especially for the proposed ADRC framework.

Due to the control-oriented scope of this study, the following applicability boundaries apply. First, the thermal framework adopts a one-way sequential electromagnetic–thermal–fluid coupling strategy. Second, the four-node LPTN is designed as a reduced-order predictor specifically for the target scenario rather than a full-envelope thermal surrogate for arbitrary operating conditions. Third, the levitation control is based on a representative single-point levitation unit rather than a more complex system.

Future work will extend to a broader range of thermal environments and operating speeds, incorporate stronger two-way coupling effects when computationally feasible, and evaluate the proposed framework in more complete multipoint or full-system levitation control scenarios.

Use of AI tools declaration

The authors declare they have not used Artificial Intelligence (AI) tools in the creation of this article.

Acknowledgments

This work was supported by the National Natural Science Foundation of China (52572416), the National Key R&D Program of China (2023YFB4302502), the Open Foundation of the State Key Laboratory of High-speed Maglev Transportation Technology (SKLM-SFCF-2024-012), and the Fundamental Research Funds for the Central Universities (22120230311).

Conflict of interest

The authors declare that they have no known competing financial interests or personal relationships that could have appeared to influence the work reported in this paper.

References

1. J. Y. Xiong, Z. G. Deng, Research progress of high-speed maglev rail transit, *J. Traffic Transp. Eng.*, **21** (2021), 177–198. https://doi.org/10.19818/j.cnki.1671-1637.2021.01.008
2. S. S. Ding, *High-Speed Maglev Transportation System at 600 km/h*, Shanghai Scientific & Technical Publishers, 2023.
3. J. D. Zhang, Q. F. Lu, Calculation and influence of cogging effect in long stator linear synchronous motors, *Trans. China Electrotech. Soc.*, **36** (2021), 964–972. https://doi.org/10.19595/j.cnki.1000-6753.tces.200875
4. C. Guo, L. Long, Y. Wu, K. Xu, H. Ye, Electromagnetic-thermal coupling analysis of a permanent-magnet in-wheel motor with cooling channels in the deepened stator slots, *Case Stud. Therm. Eng.*, **35** (2022), 102158. https://doi.org/10.1016/j.csite.2022.102158
5. J. H. Ma, Q. F. Lu, Y. X. Li, Iron loss analysis of long stator linear synchronous motors for high-speed maglev trains, *New Technol. Electr. Eng. Energy*, **42** (2023), 14–25. https://doi.org/10.12067/ATEEE2211017
6. J. Cao, X. Deng, D. Li, B. Jia, Electromagnetic analysis and optimization of high-speed maglev linear synchronous motor based on field-circuit coupling, *CES Trans. Electr. Mach. Syst.*, **6** (2022), 118–123. https://doi.org/10.30941/CESTEMS.2022.00017
7. G. Schmid, F. Schneider, F. Dignath, X. Liang, P. Eberhard, Static and dynamic modeling of the electromagnets of the maglev vehicle Transrapid, *IEEE Trans. Magn.*, **57** (2021), 1–15. https://doi.org/10.1109/TMAG.2020.3039950
8. J. Wang, X. N. Zhang, Y. F. Liu, Z. Y. Qin, L. Ma, F. F. Hong, et al., Dynamic analysis of magnetorheological damper incorporating elastic ring in coupled multi-physical fields, *Mech. Syst. Signal Process.*, **208** (2024), 111040. https://doi.org/10.1016/j.ymssp.2023.111040
9. W. Szelag, C. Jedryczka, A. Myszkowski, R. M. Wojciechowski, Coupled field analysis of phenomena in hybrid excited magnetorheological fluid brake, *Sensors*, **23** (2023), 358. https://doi.org/10.3390/s23010358
10. W. Wang, D. Yang, H. Li, Fuzzy PID maglev control based on adaptive genetic algorithm, in *Proceedings of the 2023 International Annual Conference on Complex Systems and Intelligent Science (CSIS-IAC)*, (2023), 987–992. https://doi.org/10.1109/CSIS-IAC60628.2023.10364162
11. A. Mughees, N. Mughees, S. A. Mohsin, K. Ejsmont, Enhancing stability and position control of a constrained magnetic levitation system through optimal fractional-order PID controller, *Alexandria Eng. J.*, **107** (2024), 730–746. https://doi.org/10.1016/j.aej.2024.09.022
12. Z. Q. Long, F. S. Dou, Z. Q. Wang, Y. S. Xu, X. L. Li, M. D. Zhai, Current status and prospects of high-speed maglev suspension and guidance control technology, *Frontier Sci. Technol.*, **2** (2023), 78–88. https://doi.org/10.3981/j.issn.2097-0781.2023.04.008
13. B. Zhang, Z. Ke, Z. Li, H. Shi, L. Liang, Z. Deng, Yawing stability and manipulative approach design for maglev car based on active disturbance rejection control, *Asian J. Control*, **26** (2024), 1003–1016. https://doi.org/10.1002/asjc.3246
14. H. Wang, Z. Wang, Z. Long, A modified ADRC scheme based on model information for maglev train, *Actuators*, **13** (2024), 328. https://doi.org/10.3390/act13090328

15. J. J. Hernández-Casañas, M. A. Márquez-Vera, B. D. Balderrama-Hernández, Characterization and adaptive fuzzy model reference control for a magnetic levitation system, *Alexandria Eng. J.*, **55** (2016), 2597–2607. https://doi.org/10.1016/j.aej.2016.04.032

16. Y. Yang, C. C. Huang, C. H. Dai, Z. Q. Long, An active resisting disturbance control method for high-speed maglev train with weak model dependence, *ISA Trans.*, **163** (2025), 172–183. https://doi.org/10.1016/j.isatra.2025.05.002

17. H. Wang, J. Q. Chen, Y. P. Jiang, D. Wang, Coupled electromagnetic and thermal analysis of permanent magnet rectifier generator based on LPTN, *IEEE Trans. Magn.*, **58** (2022), 1–5. https://doi.org/10.1109/TMAG.2021.3085089

18. M. H. Park, S. C. Kim, Development and validation of lumped parameter thermal network model on rotational oil spray cooled motor for electric vehicles, *Appl. Therm. Eng.*, **225** (2023), 120176. https://doi.org/10.1016/j.applthermaleng.2023.120176

19. L. He, Y. Feng, Y. Zhang, B. Tong, Methods for temperature estimation and monitoring of permanent magnet: A technology review and future trends, *J. Braz. Soc. Mech. Sci. Eng.*, **46** (2024), 174. https://doi.org/10.1007/s40430-024-04723-2

20. L. Cheng, Y. Lan, Z. Xu, Y. Sun, J. Li, Dual sliding mode control of linear maglev synchronous motor based on novel extended state observer, *Proc. Inst. Mech. Eng. Pt. I J. Syst. Control Eng.*, **238** (2024), 1171–1180. https://doi.org/10.1177/09596518241238413

21. Q. Zhu, S. M. Wang, Y. Q. Ni, A review of levitation control methods for low- and medium-speed maglev systems, *Buildings*, **14** (2024), 837. https://doi.org/10.3390/buildings14030837

22. N. Jiang, R. Cao, K. Wang, Cascaded active disturbance rejection control strategy for linear flux-switching permanent magnet motors, *IEEE Trans. Transp. Electrif.*, **11** (2025), 1396–1404. https://doi.org/10.1109/TTE.2024.3404995

23. A. Slimani, A. Bourek, A. Ammar, K. Kakouche, A. Benrabah, W. Hattab, et al., Performance enhancement of an LADRC controller using LDOB-based observers for PMSMs in electric vehicles: an experimental validation, *Electr. Eng.*, **107** (2025), 12369–12390. https://doi.org/10.1007/s00202-025-03155-y

24. A. Parkash, A. Swarup, Development of autonomous vehicle lateral control using time-varying asymmetric barrier Lyapunov function via ADRC approach, *Proc. Inst. Mech. Eng. Pt. I J. Syst. Control Eng.*, **236** (2022), 1679–1691. https://doi.org/10.1177/09596518221103040

25. Z. Wang, Z. Long, X. Li, Track irregularity disturbance rejection for maglev train based on online optimization of PnP control architecture, *IEEE Access*, **7** (2019), 12610–12619. https://doi.org/10.1109/ACCESS.2019.2891964

AIMS Press